Biosensors and Bioelectronics 298 (2026) 118411

Contents lists available at ScienceDirect

Biosensors and Bioelectronics

journal homepage: www.elsevier.com/locate/bios

A novel ratiometric biosensor based on germanene nanosheets for rapid and sensitive BRCA1 detection in differentiating T cells

Yingying Huang [a], Shu Xiao [a], Zhiming Zhong [a], Kamning Yuen [a], Bohan Yin [b,c], Jiareng Chen [a], Jiaxiang Yan [a], Jun Peng [e], Qin Zhang [a,f], Fengqi Wang [a], Bin Liu [e], Siu Hong Dexter Wong [b,c,*], Mo Yang [a,d,**]

[a] *Department of Biomedical Engineering, The Hong Kong Polytechnic University, Kowloon, Hong Kong, 999077, China*
[b] *School of Medicine and Pharmacy, Ocean University of China, Qingdao, 266003, China*
[c] *Laboratory for Marine Drugs and Bioproducts, Qingdao Marine Science and Technology Center, Qingdao, 266237, China*
[d] *Joint Research Center of Biosensing and Precision Theranostics, The Hong Kong Polytechnic University, Kowloon, Hong Kong, 999077, China*
[e] *College of Material Science and Engineering, Shenzhen University, Shenzhen, 518060, China*
[f] *Medicine School, Hunan University of Chinese Medicine, Changsha, Hunan, 410208, China*

ARTICLE INFO

Keywords:
Germanene
BRCA1 gene
FRET
Ratiometric fluorescence
$CD8^+$ T cell

ABSTRACT

The BRCA1 gene is essential for the developmental regulation and function of T lymphocytes, yet its mRNA expression during T-cell differentiation remains unclear due to the lack of effective in-situ monitoring tools. To address this, we developed a ratiometric fluorescent nanosensor based on Förster resonance energy transfer (FRET) for reliable quantification of BRCA1 mRNA in living $CD8^+$ T cells. The sensor comprises a fluorescein-labeled DNA probe (FAM_{cDNA}) assembled with Triton X-100-modified methylgermanene nanosheets (GeT), forming an efficient FRET pair. In the absence of the target, FAM_{cDNA} adsorbs onto the GeT surface, resulting in a FRET effect that quenches FAM fluorescence and enhances GeT emission by 1.63-fold. Upon specific hybridization with BRCA1 mRNA, the probe detaches, disrupting the FRET process and causing a quantitative ratiometric shift (I_{520}/I_{640}). This self-calibrating system demonstrates high sensitivity, with detection limits of 18.1 pM ($R^2 = 0.985$) for synthetic DNA and 17.2 pM ($R^2 = 0.996$) for mRNA, and a rapid response time (~10 min). Importantly, the nanoprobe enabled ratiometric imaging of endogenous BRCA1 mRNA in living $CD8^+$ T cells, revealing a significant increase in the I_{520}/I_{640} ratio during activation, visually confirming BRCA1 upregulation consistent with RNA-seq data. This work provides a robust assay for T-cell studies and highlights red-emissive germanene as a promising platform for ratiometric biosensing.

1. Introduction

The breast cancer susceptibility gene 1 (BRCA1), known for its roles in DNA repair and cancer risk (Creeden et al., 2021; Wilkinson and Gathani, 2022), exhibits critical non-canonical functions in T-cell immunity (Fu et al., 2022; Han, Y.J. et al., 2021). For instance, BRCA1 is enriched in tumor-infiltrating $CD8^+$ T cells, and its deficiency is associated with immunosuppression (Samstein et al., 2021; Wu, B. et al., 2023). However, the in-situ regulation of BRCA1 within T cells, particularly during activation and differentiation, remains poorly defined. To address this gap, in-situ tools are needed that could quantify BRCA1 mRNA directly in living immune cells with spatial resolution and accuracy.

Established assays for BRCA1 analysis, such as polymerase chain reaction (PCR)-based methods and next-generation sequencing, provide high analytical specificity and variant calling, but they are endpoint assays and are incompatible with in-situ intracellular readout (Gross et al., 1999; Tian et al., 2000; Wallace, 2016). Emerging biosensing approaches such as fluorescence (Tan et al., 2024; Wang et al., 2024), surface plasmon resonance (Šprinher et al., 2025; Yadav et al., 2024), electrochemiluminescence (Britto et al., 2024; Huo et al., 2019), and electrochemistry (Wu, J. et al., 2023; Yıldır et al., 2024) are being

---

This article is part of a special issue entitled: Biosensors 2025 published in Biosensors and Bioelectronics.

* Corresponding author. School of Medicine and Pharmacy, Ocean University of China, Qingdao, 266003, China.

** Corresponding author. Department of Biomedical Engineering, The Hong Kong Polytechnic University, Kowloon, Hong Kong, 999077, China.

E-mail addresses: dexterwong@ouc.edu.cn (S.H.D. Wong), mo.yang@polyu.edu.hk (M. Yang).

https://doi.org/10.1016/j.bios.2026.118411
Received 5 November 2025; Received in revised form 29 December 2025; Accepted 15 January 2026

developed for sensitive, selective, and rapid detection of biomarkers for disease diagnosis (Khazaei et al., 2023; Ruan et al., 2025; Sharma et al., 2024). Among these, fluorescence-based biosensors are well-suited for live-cell analysis, particularly Förster resonance energy transfer (FRET) systems employing two-dimensional (2D) nanomaterials as quenchers (Chen et al., 2022; Rohaizad et al., 2021). However, most such sensors (e.g., graphene, molybdenum disulfide (MoS_2)) rely on a single-signal "turn-on" or "turn-off" response, which compromises quantitative fidelity in complex and fluctuating cellular environments (Demchenko, 2005; Ryder et al., 2016; Yuan et al., 2015; Zhang et al., 2021).

To overcome this limitation, we engineered a ratiometric biosensor that leverages the unique photophysical properties of methyl-functionalized germanene (mGe) nanosheets. Compared to traditional 3D nanomaterials (e.g., quantum dots) and DNA probes, mGe offers a distinct set of advantages for intracellular imaging. The 2D planar structure of germanene offers a superior surface area for DNA adsorption and enables more efficient energy transfer compared to spherical nanoparticles (Ang et al., 2021). Distinct from quantum dots (often containing Cd or Pb), germanene is heavy-metal free and exhibits adequate stability for the sensing window while ensuring excellent biocompatibility through eventual degradation (Luo et al., 2023; Zhu et al., 2019). Furthermore, unlike conventional 2D quenchers, mGe possesses intrinsic tunable fluorescence, enabling it to function simultaneously as a FRET acceptor and an adsorptive quencher (Davami and Aarabi, 2024; Jiang et al., 2014). While its absolute quantum yield is modest compared to commercial dyes, this inherent signal allows for ratiometric designs, enabling self-calibration to cope with environmental fluctuations, which significantly improves imaging fidelity and robustness (Huang et al., 2018; Li et al., 2025).

In this work, we report the design and synthesis of a germanene-based ratiometric nanoprobe (GeT/FAM$_{mRNA}$) for the amplification-free in-situ detection of BRCA1 mRNA in differentiating T cells (Fig. 1). The sensing mechanism is based on the competitive displacement of a FAM-labeled DNA probe from the nanosheet surface upon hybridization with the target BRCA1 sequence. This process disrupts FRET, causing a reciprocal change in the fluorescence of the FAM donor (520 nm) and the germanene acceptor (640 nm). The resulting nanoprobe demonstrated exceptional specificity against mismatch sequences and picomolar sensitivity for both BRCA1 DNA (LOD = 18.1 pM) and mRNA (LOD = 17.2 pM) within 10 min. Critically, we establish the utility of this platform in a biologically relevant context by successfully quantifying the upregulation of endogenous BRCA1 mRNA inside living

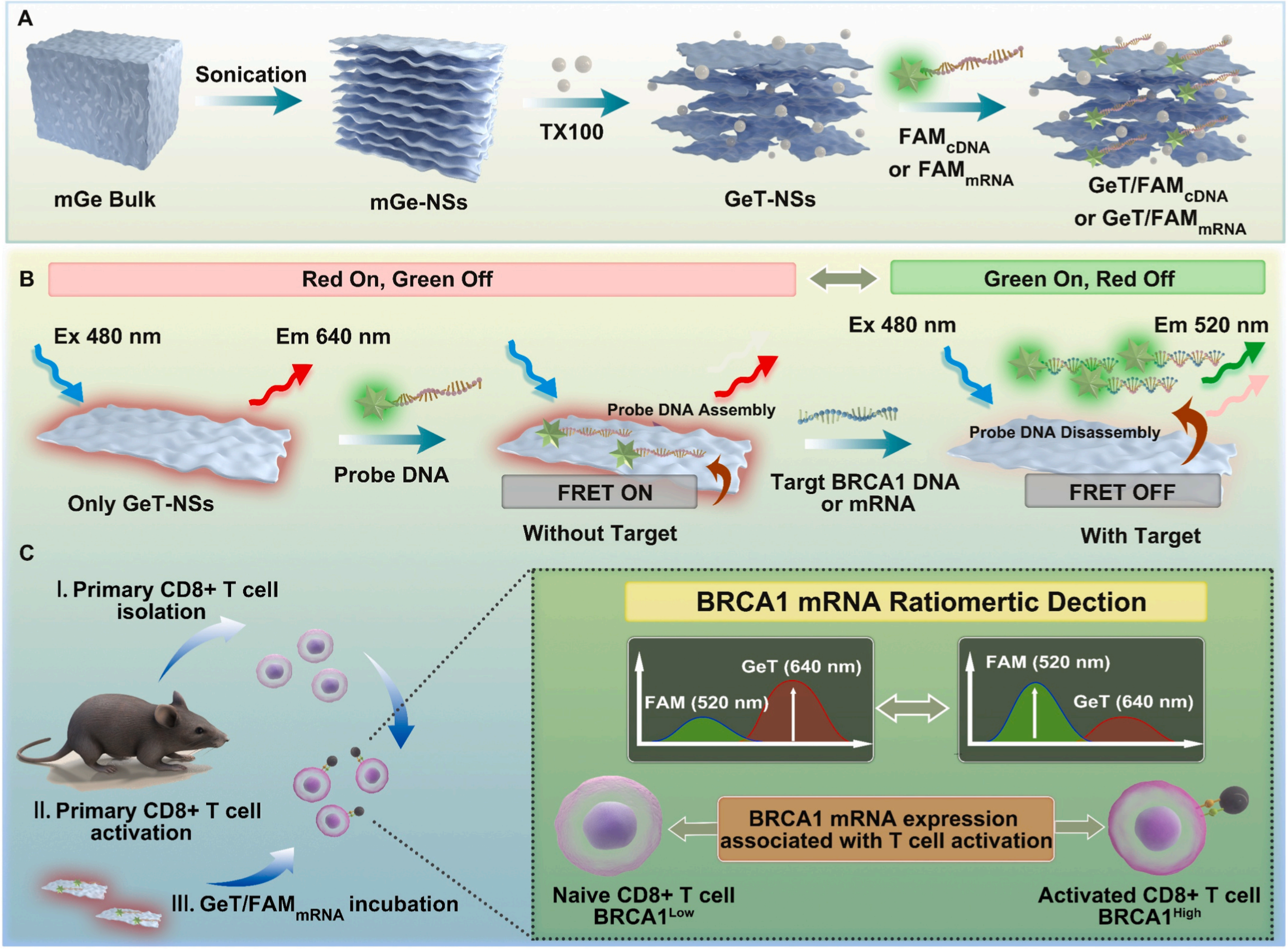

Fig. 1. Schematic illustration of ratiometric fluorescent BRCA1 biosensor preparation and mechanism. (A) Preparation route of the GeT/FAM$_{cDNA}$ or GeT/FAM$_{mRNA}$ nanoprobe. FAM-labeled cDNA or mRNA physically adsorbs onto GeT nanosheets through hydrophobic interactions. (B) BRCA1 detection mechanism. Without target: FAM$_{cDNA}$ adsorption enables FRET, enhancing GeT emission (red on) while quenching FAM fluorescence (green off). With BRCA1 target: cDNA hybridizes with mRNA, desorbing from GeT to terminate FRET, restoring FAM fluorescence (green on) and reducing GeT emission (red off). (C) Proposed application for T cell monitoring. Schematic representation of GeT/FAM$_{cDNA}$ nanoprobe deployment to track BRCA1 mRNA expression in primary murine CD8$^+$ T cells during ex vivo activation with CD3/CD28 Dynabeads™. (For interpretation of the references to colour in this figure legend, the reader is referred to the Web version of this article.)

CD8$^+$ T cells during activation. This work establishes germanene-based ratiometric biosensing as a powerful and reliable platform for investigating in-situ gene expression and holds significant promise for future applications in diagnostics.

2. Experimental section

The part of materials and methods demonstrates in the file of **supplementary information**.

3. Results and discussion

3.1. Synthesis and characterization of GeT-NSs

We synthesized few-layered methylgermanene nanosheets (mGe-NSs) via liquid-phase sonication of a bulk precursor in 1% Triton X-100 (TX-100) to yield colloidally stable GeT-NSs (Xue et al., 2020). Electron microscopy and dynamic light scattering (DLS) analysis revealed that the lateral dimensions of the nanosheets could be systematically controlled by sonication duration, decreasing from ~2 μm to ~200 nm over 1–4 h (Fig. 2A–D, Fig. S1, and Fig. S2A). This was accompanied by a reduced zeta potential (−15.8 mV to −3.52 mV), attributed to increased surfactant coverage (Fig. S2B). It was observed that increasing the duration of ultrasonic treatment led to a gradual decrease in the size of the nanosheet samples, along with a reduction in polydispersity index (PDI) (Fig. S2C). For our sensing experiments, we selected GeT-NSs subjected to 4 h of ultrasonic treatment, which exhibited an average hydrodynamic diameter of approximately 300 nm and a low PDI of 0.192. This low PDI (<0.2) reflects a narrow size distribution and excellent colloidal homogeneity, making these nanosheets highly suitable for consistent and reliable FRET-based sensing. A 4-h sonication was optimal, producing uniform nanosheets of 100–200 nm lateral size and ~5.2 nm thickness, as measured by atomic force microscopy (AFM) (Fig. 2E). High-resolution TEM (HRTEM) images confirmed their high crystallinity, revealing the 0.202 nm lattice spacing of the (220) crystal plane (Fig. 2F).

X-ray diffraction (XRD) patterns of both the bulk mGe and the exfoliated GeT-NSs exhibited identical characteristic peaks for the (111), (220), (400), and (422) crystal planes, confirming that the exfoliation process preserves the intrinsic crystalline structure of the material (Fig. 3A). Concurrently, Raman spectroscopy revealed a pronounced blue shift of the primary vibrational mode from 301 cm^{-1} to 266 cm^{-1}, indicating dimensional confinement (Fig. 3B) (Li et al., 2014). The optical properties of the GeT-NSs also exhibited clear size-dependence. UV–Vis extinction decreased with size, while quantum confinement effects widened the band gap from 2.44 eV to 2.75 eV, causing a corresponding blue shift in fluorescence emission(Fig. 3C–D) (Backes et al., 2014, 2016).These results demonstrate the tunable optoelectronic properties of GeT-NSs, a hallmark of quantum confinement in 2D materials (Jia et al., 2019).

Given their potential for sensing applications, we systematically evaluated the photophysical properties and stability of the GeT-NSs. The GeT-NSs demonstrated key properties for quantitative sensing, including excitation-wavelength-independent fluorescence and a linear concentration-dependent emission (Fig. 3E–F). The TX-100 passivation conferred excellent colloidal and fluorescence stability, with GeT-NSs retaining 35% more emission than non-stabilized counterparts over 10 h (Fig. S3). The nanosheets also showed excellent photostability across various common laboratory solvents and at a physiological temperature of 37 °C (Fig. S4). Furthermore, the fluorescence signals of GeT-NSs remained stable across the pH range of 6.5–7.4, demonstrating the probe's suitability for intracellular measurements in differentiating T cells, which typically exhibit an intracellular pH of approximately 6.5 (Fig. S5) (Huang et al., 2024). These findings confirm GeT-NSs possess the stable photoluminescence required for a reliable biosensing platform.

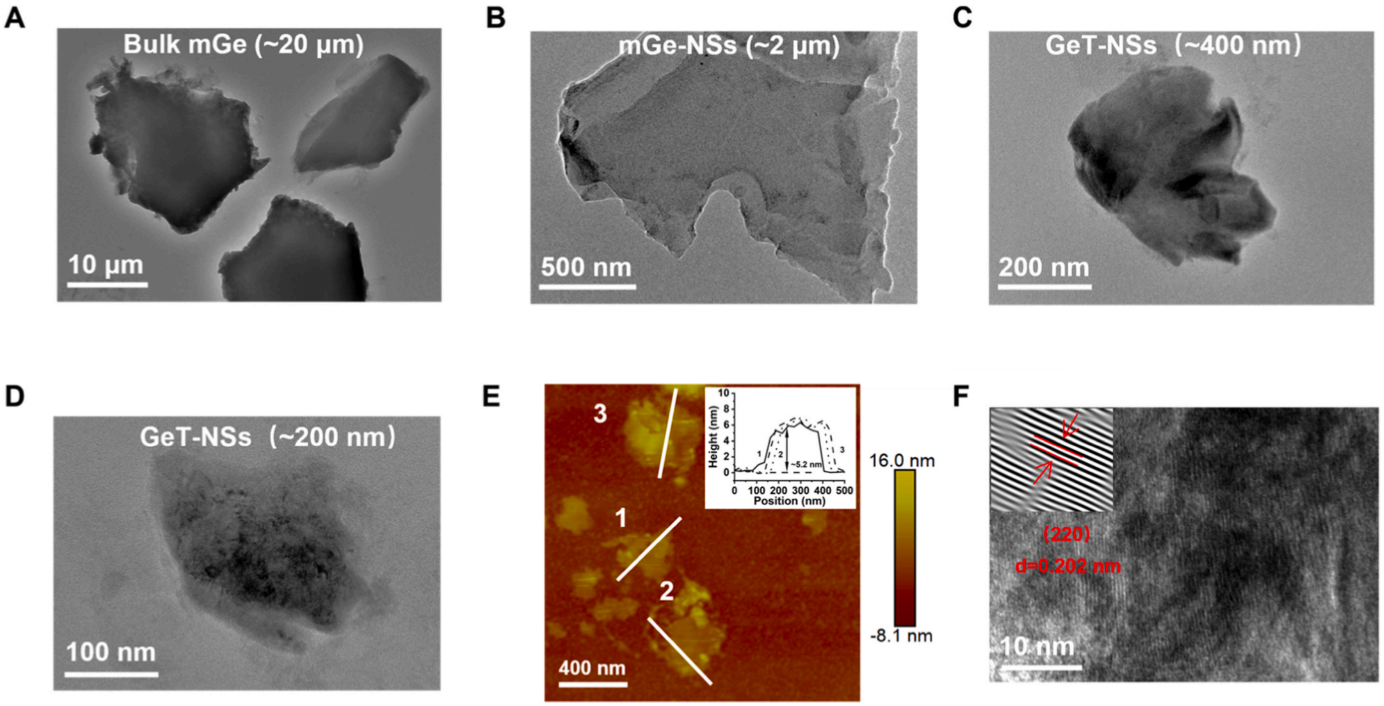

Fig. 2. Morphological characterization and structural analysis of GeT-NSs during surfactant-assisted exfoliation. (A, B) TEM image of (A) Bulk mGe prior to exfoliation, (B) mGe-NSs following 6 h of sonication in NMP. (C, D) TEM images of GeT-NSs after further exfoliation in TX-100 solution for (C) 3 h sonication (~400 nm lateral dimensions), and (D) 4 h sonication (~200 nm lateral dimensions). (E) AFM topography and the corresponding height profile along the three white lines shown in the *inset*, indicating a GeT-NS thickness of ~5.2 nm. (F) HR-TEM image of a representative ~200 nm GeT-NS. *Inset*: interplanar spacing analysis using DigitalMicrograph™ software. Scale bars: 10 μm (A), 500 nm (B), 200 nm (C), 100 nm (D), 400 nm (E), 10 nm (F).

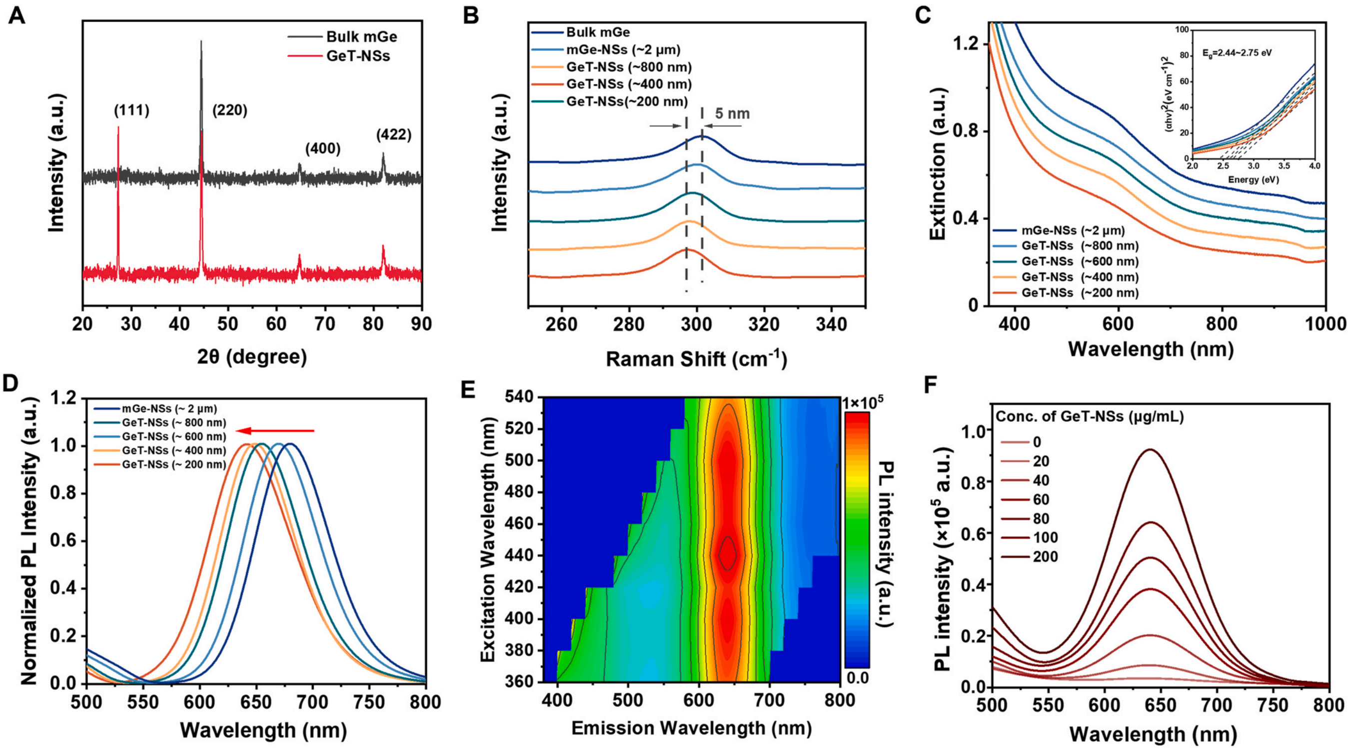

Fig. 3. Size-dependent optical properties of GeT-NSs. (A) XRD patterns comparing the crystal structure of bulk mGe with that of the exfoliated GeT-NSs. (B) Raman spectra for bulk mGe and size-varied GeT-NSs. (C) Extinction spectra of GeT-NSs with different sizes. *Inset*: Tauc plot for band gap determination $(\alpha h\nu)^{\frac{1}{n}} = B(h\nu - Eg)$, where α = absorption coefficient, h = Planck's constant, ν = frequency, B = constant, Eg = band gap ($n = 1/2$ for direct, 2 for indirect transitions). (D) Normalized photoluminescence (PL) emission spectra of different-sized GeT-NSs (Ex: 480 nm). (E) Excitation-emission matrix (EEM) profiles (Ex: 360–540 nm, 20 nm intervals). (G) Concentration-dependent PL emission spectra of ~200 nm GeT-NSs, measured over a range of 0–200 μg/mL (Ex: 480 nm).

3.2. Assembly and mechanistic characterization of GeT/FAM$_{cDNA}$ nanoprobe

The GeT/FAM$_{cDNA}$ nanoprobe was constructed by adsorbing FAM$_{cDNA}$ onto the surface of GeT-NSs via non-covalent interactions. Detailed sequences of the DNA oligonucleotides are listed in Table S1. The average height of nanosheets increased from ~5.2 nm (bare GeT) (Fig. 2E) to ~7.2 nm (GeT/FAM$_{cDNA}$) (Fig. S6). This ~2.0 nm height increase corresponds to the theoretical diameter of single-stranded DNA, confirming the successful adsorption of DNAs on the nanosheet surface (Morimitsu et al., 2022; Zhang et al., 2023a). The assembly was designed as a FRET pair, with the FAM$_{cDNA}$ donor (emission = 520 nm) and the GeT-NSs acceptor (broad absorption, 300–700 nm) exhibiting significant spectral overlap (Fig. 4A). This enabled efficient FRET, resulting in strong quenching of FAM fluorescence and a concurrent 1.63-fold enhancement of the GeT-NSs emission at 640 nm (Fig. 4B). By titrating a fixed concentration of FAM$_{cDNA}$ (10 nM) against increasing amounts of GeT-NSs, we determined an optimal concentration of GeT-NSs was 100 μg/mL, at which the quenching efficiency was 82.5 ± 5.6% (Fig. 4C–D).

To elucidate the adsorption mechanism, we conducted a competitive binding assay using four agents representing distinct intermolecular forces: urea (hydrogen bonding), 1,6-hexanediol (hydrophobic interactions), NaCl (electrostatic interactions), and guanine (π-π stacking) (Fig. 4E). Significant fluorescence recovery was observed upon introducing 1,6-hexanediol, guanine, and NaCl, whereas urea showed negligible effect (Fig. 4F). While the desorption triggered by NaCl might suggest electrostatic involvement, direct electrostatic adsorption is unlikely as both GeT and FAM$_{cDNA}$ are negatively charged; instead, high ionic strength likely alters the solvation shell or the conformation of surface-adsorbed TX-100. This result demonstrates that the adsorption of DNA onto GeT-NSs is primarily driven by hydrophobic interactions and π-π stacking between DNA bases and the nanosheet surface. This mechanism is analogous to the van der Waals force-dominated adsorption observed on graphene and other 2D nanomaterials like MoS$_2$ (Reza Rezapour and Biel, 2022; Zhang et al., 2023b). For the sensing system, optimal binding strength is crucial, as it ensures stable association for reliable FRET sensing while allowing necessary molecular interactions for effective sensor performance. We further evaluated the binding interaction between DNA and GeT surface via the Stern-Volmer quenching constant (*Ksv*) curve. The *Ksv* was determined to be 3.1 × 10^3 M^{-1}, indicating an enough affinity sufficient to prevent leakage but allowing for specific displacement by the target DNA (Fig. S7).

To confirm that FRET was the dominant quenching mechanism and to rule out contributions from the inner filter effect (IFE), we measured the fluorescence lifetime (τ) of FAM$_{cDNA}$. The lifetime of FAM$_{cDNA}$ decreased sharply from 2.01 ± 0.24 ns (free) to 0.18 ± 0.05 ns (complexed with GeT-NSs) (Fig. 4G). This reduction is definitive evidence of FRET, as IFE does not alter excited-state lifetime (Tang et al., 2019). Furthermore, the UV–Vis absorption spectrum of the GeT/FAM$_{cDNA}$ complex was a simple superposition of its components (Fig. 4H), confirming a dynamic quenching process governed by non-covalent interactions rather than static ground-state complex formation.

3.3. Ratiometric detection of BRCA1 DNA and mRNA in solution

We next evaluated the performance of the GeT/FAM$_{cDNA}$ nanoprobe for the ratiometric detection of BRCA1 DNA and mRNA. The sensing mechanism relies on hybridization-induced desorption: a complementary BRCA1 target hybridizes with the FAM$_{cDNA}$ probe, forming a rigid duplex that desorbs from the nanosheet surface. This desorption restores FAM fluorescence at 520 nm while simultaneously diminishing GeT-NSs emission at 640 nm as FRET ceases, enabling a ratiometric response (I_{520}/I_{640}). Probes targeting BRCA1 DNA (GeT/FAM$_{cDNA}$) and mRNA

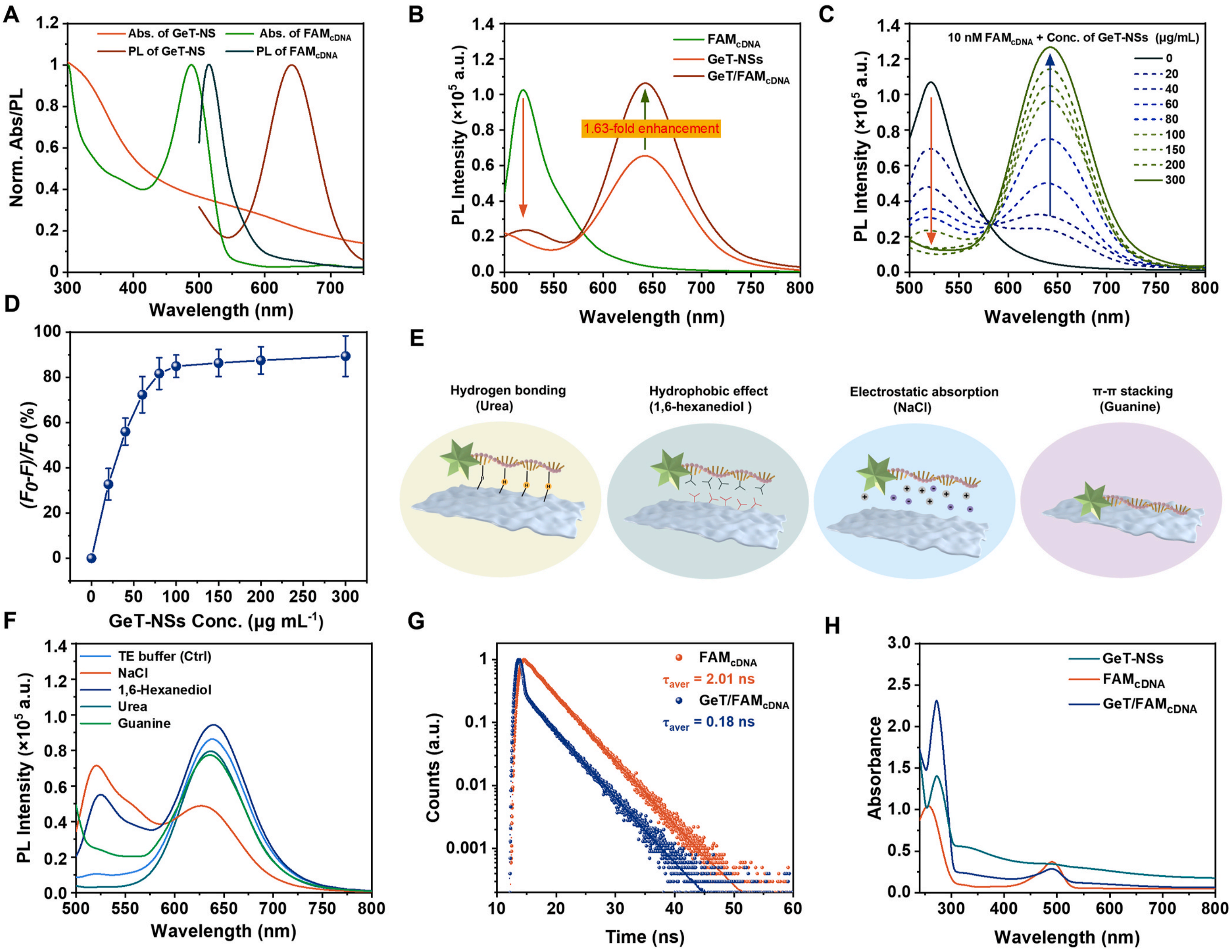

Fig. 4. Evaluation of the fluorescence quenching mechanism for the GeT/FAM$_{cDNA}$ probe. (A) Spectral overlap between the PL emission of GeT-NSs (acceptor) and the UV–vis absorption of FAM-labeled cDNA (donor). (B) PL spectra of GeT-NSs before and after FAM$_{cDNA}$ adsorption, demonstrating the FRET effect. (C) PL spectra of FAM$_{cDNA}$ (10 nM) titrated with increasing concentrations of GeT-NSs (0–300 μg/mL), Ex: 480 nm. (D) FAM$_{cDNA}$ fluorescence quenching efficiency versus GeT-NS concentration, derived from (C). (E) Proposed non-covalent interactions enabling GeT/FAM$_{cDNA}$ complex formation: hydrogen bonding, hydrophobic effects, electrostatic forces, and π-π stacking. (F) Competitive binding assays: PL recovery of GeT/FAM$_{cDNA}$ after adding disruptors (2.5 M NaCl: electrostatic; 0.8 M 1,6-hexanediol: hydrophobic; 1.6 M urea: H-bonding; 350 mM guanine: π-π stacking). (G) Time-resolved fluorescence decay curves for FAM$_{cDNA}$ with/without GeT-NSs. (H) UV–vis absorption spectra of GeT-NSs, FAM$_{cDNA}$, and the resulting GeT/FAM$_{cDNA}$ complex.

(GeT/FAM$_{mRNA}$) were prepared, and the ratiometric signal was found to stabilize within 10 min, which was adopted as the standard incubation time (Fig. S8). Under optimized conditions, the probe for BRCA1 DNA exhibited a strong linear correlation ($R^2 = 0.985$) in the 0–50 nM range, with a limit of detection (LOD) of 18.1 pM (Fig. 5A–B). The platform was equally effective for BRCA1 mRNA, showing a similar linear response ($R^2 = 0.996$) and an LOD of 17.2 pM (Fig. 5C–D). To visualize the sensing process, we used an in vivo imaging system (IVIS) to image multiwell plates containing the nanoprobe and varying concentrations of the BRCA1 target (Fig. 5E–G). As the BRCA1 concentration increased, the signal in the FAM channel (520 nm) intensified while the signal in the GeT-NSs channel (640 nm) diminished, providing clear visual confirmation of the concentration-dependent ratiometric response in a high-throughput format (Fig. 5H).

Finally, we performed several control experiments to validate the proposed mechanism and selectivity of the nanoprobe. Agarose gel electrophoresis confirmed that fluorescence recovery was due to hybridization, as evidenced by a band shift corresponding to the formed FAM$_{cDNA}$-BRCA1 duplex (Fig. S9). We measured the selectivity of GeT/FAM$_{mRNA}$ against other mRNAs and non-coding RNAs (e.g., miR-155 and miR-150) (Chen et al., 2017; Gracias et al., 2013). While a strong signal was observed for the specific BRCA1 target, the response to non-complementary sequences, single- or double-base mismatches, and other interferents remained negligible (Fig. 5I). These results confirm that only perfectly complementary sequences form stable duplexes with sufficient binding energy to overcome probe-GeT-NSs adsorption, thereby enabling significant fluorescence recovery. In contrast, the presence of mismatches destabilizes the duplex structure, impeding probe detachment from the GeT-NSs surface and resulting in minimal fluorescence changes.

We further evaluated the stability of the GeT/FAM$_{mRNA}$ probe in complex biological and ionic settings. The fluorescence intensity ratio (I_{520}/I_{640}) exhibited negligible fluctuation in serum-containing environments (Fig. S10A). Similarly, the ratio remained unchanged in the presence of physiological sodium and potassium ion concentrations but increased significantly upon target DNA hybridization. These results confirm that the nanoprobe maintains its stability and specificity without interference from physiological ionic conditions (Fig. S10B). Notably, comparative analysis confirmed the platform's superior performance, including lower detection limits and faster response times,

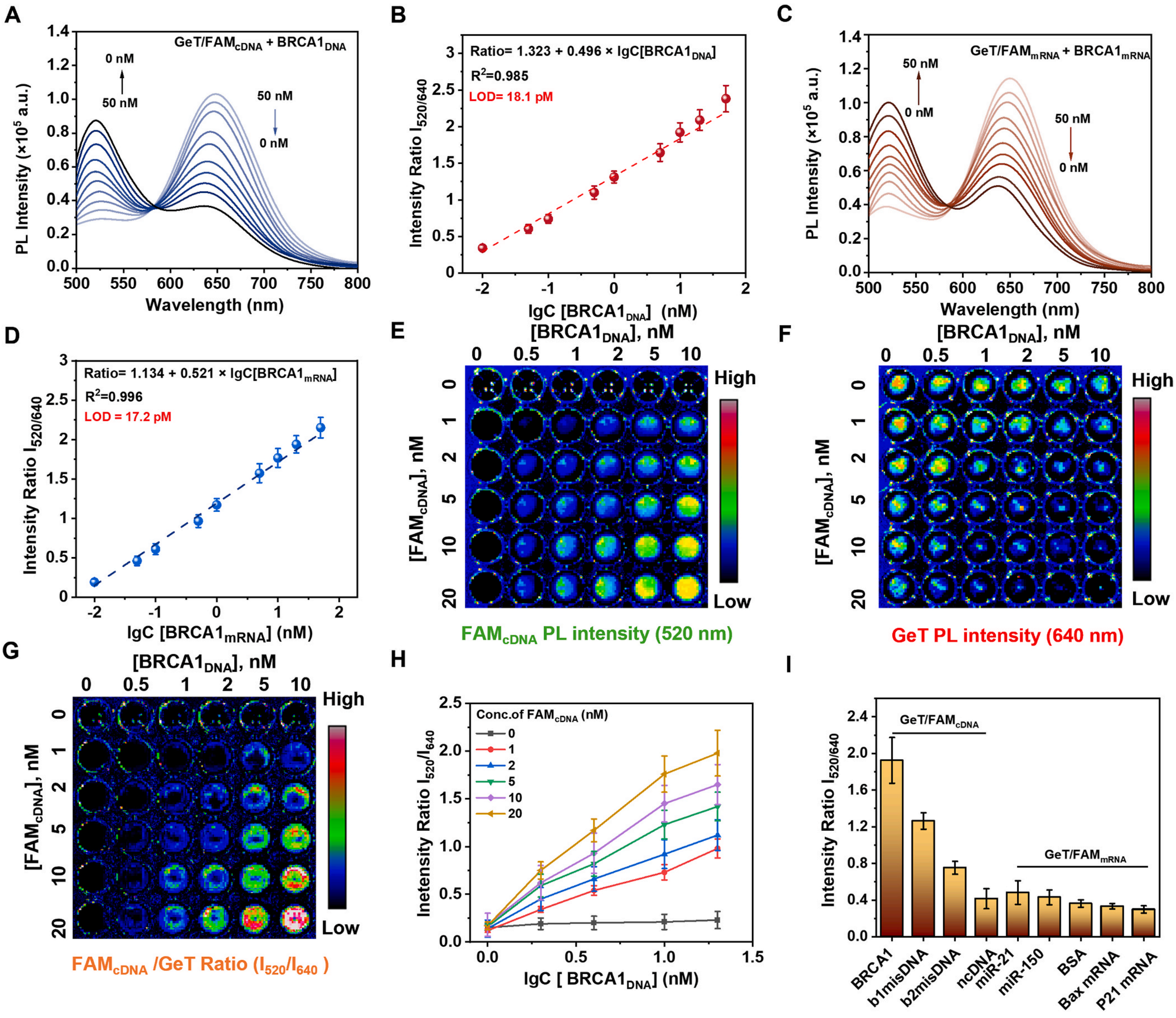

Fig. 5. Ratiometric detection of BRCA1 DNA/mRNA sequences by the GeT/FAM$_{cDNA}$ or GeT/FAM$_{mRNA}$ nanoprobe in solution. (A) PL spectra of the nanoprobe (10 nM) after hybridization with BRCA1 DNA (0, 0.01, 0.05, 0.1, 0.5, 1, 10, 20, 50 nM). (B) Linear correlation between ratiometric intensity (I$_{520}$/I$_{640}$) and log$_{10}$ [BRCA1 DNA] (nM); LOD indicated. (C) PL spectra of the nanoprobe (10 nM) with BRCA1 mRNA (0, 0.01, 0.05, 0.1, 0.5, 1, 10, 20, 50 nM). (D) Linear correlation between ratiometric intensity (I$_{520}$/I$_{640}$) and log$_{10}$ [BRCA1 mRNA] (nM); LOD indicated. The limit of detection (LOD) was calculated using the formula: $LOD = 3.3\theta/\ K,$ where θ is the standard deviation of the blank signal (n = 3) and K is the slope of the linear calibration curve. (E, F) Fluorescence images of a multiwell plate with increasing GeT/FAM$_{cDNA}$ concentrations (left to right, 0–10 nM BRCA1 target) and FAM$_{cDNA}$ probe concentrations (top to bottom, 0–20 nM) in TE buffer (pH 7.4, 25 °C). Images acquired after 30 min incubation using: (E) FAM channel (Ex: 480 ± 20 nm, Em: 520 ± 20 nm); (F) GeT-NS channel (Ex: 480 ± 20 nm, Em: 620 ± 20 nm). (G) Ratiometric images (FAM/GeT intensity ratio) derived from (E, F). (H) A plot of I$_{520}$/I$_{640}$ ratio with different BRCA1 concentrations. (I) Fluorescence intensity ratios (I$_{520}$/I$_{640}$) of the nanoprobe with BRCA1 target DNA (10 nM), control sequences (b1misDNA, b2misDNA, ncDNA; 10 nM), BSA (50 nM) and non-target RNAs (miR-21, miR-150, miR-155, Bax mRNA, P21 mRNA; 50 nM).

relative to established methods (Table S2). These results establish the nanoprobe as a highly selective and sensitive platform for BRCA1 detection.

3.4. Intracellular detection of BRCA1 mRNA in living activated CD8$^+$ T cells

To demonstrate its biological utility, the nanoprobe was applied to monitor BRCA1 mRNA during the *in vitro* activation of murine CD8$^+$ T cells. Following established protocols (Huang et al., 2024), we isolated naive CD8$^+$ T cells from murine spleens and stimulated them with CD3/CD28 Dynabeads™ to induce activation. The stimulation triggered robust cell proliferation, with the cell count increasing from 3 × 10^4 to 1.7 × 10^5 cells/mL within the first 24 h and continuing to expand over time. In contrast, the non-activated control group stagnated and eventually declined in number (Fig. S11). We then used flow cytometry to characterize the activated T cells. Flow cytometry analysis confirmed that the CD3/CD28 stimulation successfully drove the differentiation of naive T cells into effector (T$_E$) and central memory (T$_{CM}$) populations, with T$_{CM}$ cells constituting 90 ± 2.5% of the culture by day 7 (Fig. S12).

To confirm the relevance of BRCA1 in this process, we performed RNA-sequencing on T cells at different activation stages (Day 0, 3, and 7) (Fig. 6A–B). The analysis revealed a significant upregulation of BRCA1 and its associated DNA-repair pathway genes (e.g., RAD50, RAD51, RAD51C, and CHEK2), alongside the downregulation of its transcriptional repressors (e.g., BACH1). This transcriptomic evidence suggests a

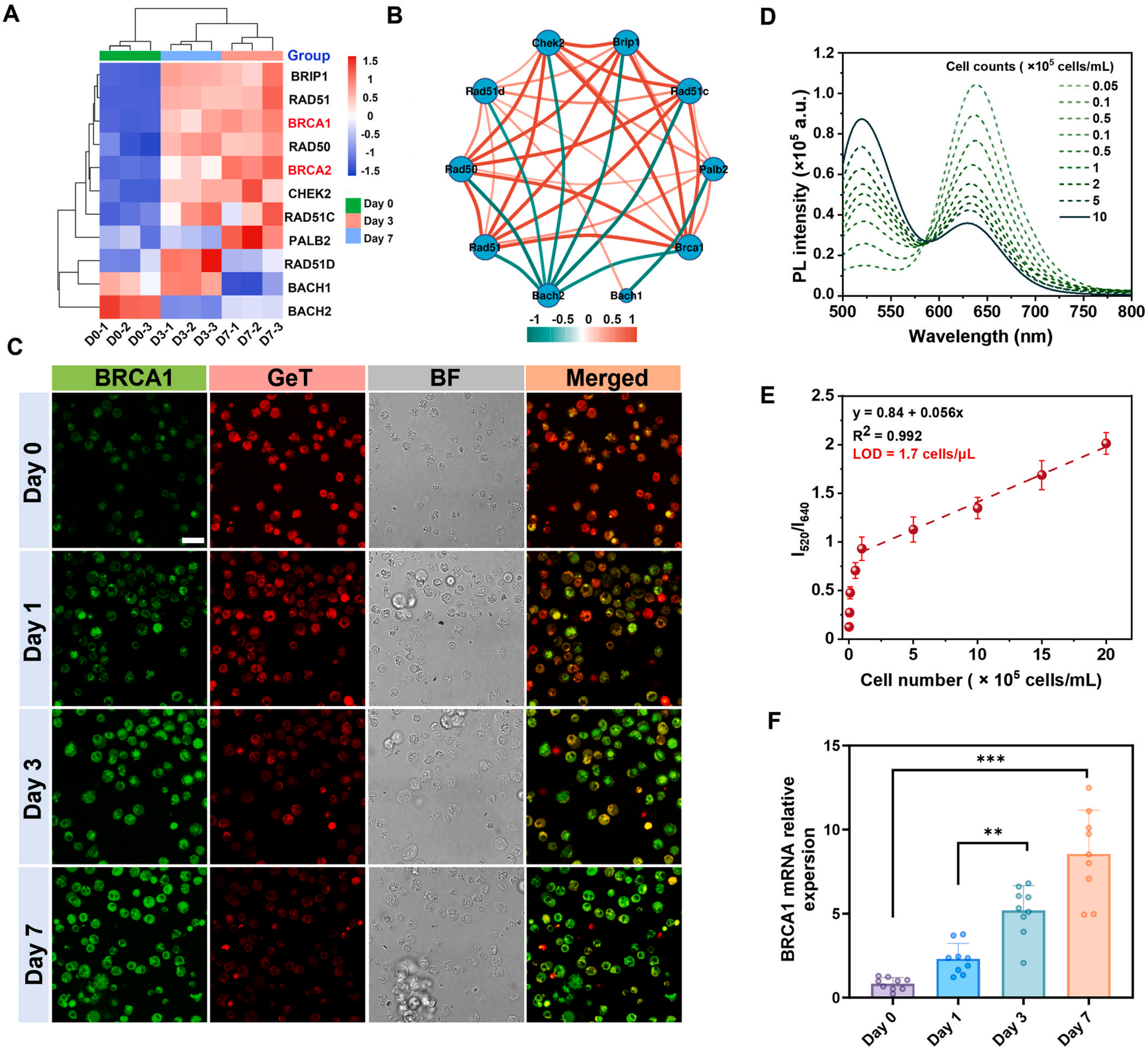

Fig. 6. In-situ BRCA1 mRNA detection in activated CD8$^+$ T cells using the GeT/FAM$_{\text{mRNA}}$ nanoprobe. (A) Heatmap of BRCA1/2-associated gene expression clusters in CD8$^+$ T cells during activation (Day 0, 3, 7). Color scale: blue (low) to red (high) expression. (B) Gene correlation network: line thickness proportional to correlation coefficient; red = positive, green = negative. (C) Confocal microscopy images of CD8$^+$ T cells (Day 0/1/3/7) after 4 h incubation with GeT/FAM$_{\text{mRNA}}$ nanoprobe. Channels: BRCA1/FAM (green; Ex: 488 nm, Em: 500–550 nm), GeT (red; Ex: 488 nm, Em: 600–700 nm), merged (FAM + GeT), bright field (BF). Scale bar: 20 μm. (D) PL spectra of cell lysates (5 × 10^3–10^5 cells) hybridized with GeT/FAM$_{\text{mRNA}}$ nanoprobe. (E) Linear correlation between cell number and ratiometric intensity (I_{520}/I_{640}); LOD shown. (F) temporal profile in relative BRCA1 mRNA expression (normalized to Day 0; mean ± SD, n = 3, **p < 0.01, ***p < 0.001). (For interpretation of the references to colour in this figure legend, the reader is referred to the Web version of this article.)

crucial role for BRCA1 in T cells activation and memory formation. Prior to intracellular imaging, we evaluated the biological suitability of the nanoprobe. Cytotoxicity assays confirmed high biocompatibility, with cell viability maintained above 90% (Fig. S13). Consistent with this, a lactate dehydrogenase (LDH) release assay showed negligible leakage compared to the TX-100 positive control, confirming that the nanoprobe preserves membrane integrity (Fig. S14). We next performed time-lapse fluorescence imaging to monitor BRCA1 mRNA in activated T cells (Fig. S15A). The T cells exhibited a significant increase in green fluorescence over time, which is attributed primarily to the upregulation of BRCA1 mRNA upon activation. Based on the cellular uptake kinetics, we identified a 4-h incubation as the optimal duration for maximum intracellular accumulation (Fig. S15B–C). Using this timeline, we further investigated the intracellular fate and uptake mechanism. Co-staining with LysoTracker Red revealed Pearson's correlation coefficient (PCC) of 0.51 at 4 h. This moderate correlation (PCC<0.7) indicates that the nanoprobe successfully escapes from endosomes/lysosomes into the cytoplasm to hybridize with target mRNA (Fig. S16) (Han, C. et al., 2021). We further utilized specific inhibitors to elucidate the entry pathway. While Nystatin (caveolin-mediated inhibitor) had minimal impact, treatment with chlorpromazine (CPZ, clathrin-mediated inhibitor) caused a significant reduction in fluorescence. Specifically, the ratiometric signal ($I_{\text{BRCA1}}/I_{\text{GeT}}$) dropped approximately 2.5-fold (Fig. S17). Collectively, these data confirm that the nanoprobe enters cells primarily via active, clathrin-mediated endocytosis, rather than through passive diffusion caused by membrane disruption.

With these optimized parameters, live naive (Day 0) and activated (Day 1, 3, 7) CD8$^+$ T cells were incubated with the GeT/FAM$_{\mathrm{mRNA}}$ nanoprobe. Confocal microscopy imaging revealed a progressive increase in the green FAM channel (500–550 nm) and a corresponding decrease in the red GeT-NSs channel (600–700 nm) as activation progressed (Fig. 6C). This ratiometric shift, visualized by the merged images transitioning from orange to green, directly indicates an upregulation of intracellular BRCA1 mRNA. To verify signal stability, we monitored naïve CD8$^+$ T cells (fixed post-incubation) over 3 days. The ratiometric signal remained stable for the 3 days without any nonspecific fluorescence increase (Fig. S18), ensuring reliable detection within our detection window. To quantify the nanoprobe's sensitivity in a cellular context, we prepared lysates from activated T cells and observed a linear, dose-dependent increase in the I_{520}/I_{640} ratio. This analysis showed the nanoprobe could detect the mRNA content from as few as 2000 cells/mL, which corresponds to approximately 2 cells per μL (Fig. 6E). Normalizing the ratiometric signal to the Day 0 baseline confirmed a statistically significant increase in BRCA1 mRNA expression from Day 3 onward, correlating positively with T cell activation (Fig. 6F). These results validate the efficacy of our nanoprobe for quantitative intracellular mRNA analysis and imaging.

4. Conclusions

In conclusion, we have successfully developed and validated a ratiometric FRET nanosensor for the dynamic, in situ monitoring of BRCA1 mRNA in living T cells. The innovation of this platform lies in the unprecedented use of methyl-functionalized germanene as both a red-emissive FRET acceptor and an adsorptive nanoquencher. This unique dual functionality enables a self-calibrating sensing mechanism that translates the specific hybridization of BRCA1 mRNA into a robust ratiometric fluorescence signal (I_{520}/I_{640}), ensuring high reliability against environmental fluctuations. By applying this high-sensitivity, amplification-free tool, we provided direct visual evidence that BRCA1 mRNA is significantly upregulated during CD8$^+$ T cells activation, corroborating its crucial role in immune cell function and differentiation. This work establishes emissive 2D germanene as a versatile platform for the design of next-generation ratiometric biosensors. Notably, the quantum confinement effect of mGe enables emission tuning, paving the way for future multiplexed detection of different mRNA targets by employing nanosheets of varying lateral sizes, each functionalized with specific probes. The principles demonstrated here open promising avenues for studying gene expression dynamics in biological systems.

CRediT authorship contribution statement

Yingying Huang: Writing – original draft, Software, Methodology, Formal analysis, Data curation, Conceptualization. **Shu Xiao:** Methodology, Investigation. **Zhiming Zhong:** Methodology, Investigation. **Kamning Yuen:** Methodology, Investigation. **Bohan Yin:** Validation, Methodology. **Jiareng Chen:** Validation, Resources. **Jiaxiang Yan:** Methodology, Investigation. **Jun Peng:** Software, Methodology. **Qin Zhang:** Methodology, Investigation. **Fengqi Wang:** Methodology, Investigation. **Bin Liu:** Methodology, Investigation. **Siu Hong Dexter Wong:** Writing – review & editing, Validation, Supervision, Project administration, Funding acquisition. **Mo Yang:** Writing – review & editing, Visualization, Supervision, Project administration, Funding acquisition.

Declaration of competing interest

The authors declare that they have no known competing financial interests or personal relationships that could have appeared to influence the work reported in this paper.

Acknowledgments

We acknowledge the support of the University Research Facility in Chemical and Environmental Analysis (UCEA) and University Research Facility in Life Sciences (ULS) of the Hong Kong Polytechnic University (PolyU). This work was supported by the Shenzhen Science and Technology Program-Basic Research Scheme (JCYJ20220531090808020), the Hong Kong Research Grants Council (RGC) Collaborative Research Fund (C5005-23W and C5078-21E), the Research Grants Council (RGC) Hong Kong General Research Fund (15217621 and 15216622), the Hong Kong Polytechnic University Internal Fund (1-YWB4, 1-WZ4E, 1-CD8M, 1-WZ4E, 1-CEB1, 1-YWDU, 1-CE2J, 1-CDKU and 1-W02C). This work was also supported by Start-up Fundings of Ocean University of China (862401013154 and 862401013155), Laboratory for Marine Drugs and Bioproducts Qingdao Marine Science and Technology Center (LMDBCXRC202401 and LMDBCXRC202402), Taishan Scholar Youth Expert Program of Shandong Province (tsqn202306102 and tsqn202312105), and Shandong Provincial Overseas Excellent Young Scholar Program (2024HWYQ-042 and 2024HWYQ-043) for supporting this work.

Appendix A. Supplementary data

Supplementary data to this article can be found online at https://doi.org/10.1016/j.bios.2026.118411.

Data availability

Data will be made available on request.

References

Ang, W.L., Sturala, J., Antonatos, N., Sofer, Z., Bonanni, A., 2021. Effect of surface chemistry on bio-conjugation and bio-recognition abilities of 2D germanene materials. Nanoscale 13 (3), 1893–1903.

Backes, C., Paton, K.R., Hanlon, D., Yuan, S., Katsnelson, M.I., Houston, J., Smith, R.J., McCloskey, D., Donegan, J.F., Coleman, J.N., 2016. Spectroscopic metrics allow in situ measurement of mean size and thickness of liquid-exfoliated few-layer graphene nanosheets. Nanoscale 8 (7), 4311–4323.

Backes, C., Smith, R.J., McEvoy, N., Berner, N.C., McCloskey, D., Nerl, H.C., O'Neill, A., King, P.J., Higgins, T., Hanlon, D., Scheuschner, N., Maultzsch, J., Houben, L., Duesberg, G.S., Donegan, J.F., Nicolosi, V., Coleman, J.N., 2014. Edge and confinement effects allow in situ measurement of size and thickness of liquid-exfoliated nanosheets. Nat. Commun. 5 (1), 4576.

Britto, J.S., Guan, X., Tran, T.K.A., Lei, Z., Bahadur, R., Patel, V., Zhang, X., Wong, S.L., Vinu, A.J.S.S., 2024. Emerging multifunctional carbon-nanomaterial-based biosensors for cancer diagnosis. Small Sci. 4 (3), 2300221.

Chen, J., Oudeng, G., Feng, H., Liu, S., Li, H.-W., Ho, Y.-P., Chen, Y., Tan, Y., Yang, M., 2022. 2D MOF nanosensor-integrated digital droplet microfluidic flow cytometry for in situ detection of multiple miRNAs in single CTC cells. Small 18 (32), 2201779.

Chen, Z., Stelekati, E., Kurachi, M., Yu, S., Cai, Z., Manne, S., Khan, O., Yang, X., Wherry, E.J., 2017. miR-150 regulates memory CD8 T cell differentiation via c-Myb. Cell Rep. 20 (11), 2584–2597.

Creeden, J.F., Nanavaty, N.S., Einloth, K.R., Gillman, C.E., Stanbery, L., Hamouda, D.M., Dworkin, L., Nemunaitis, J., 2021. Homologous recombination proficiency in ovarian and breast cancer patients. BMC Cancer 21 (1), 1154.

Davami, A., Aarabi, M., 2024. Effect of MoS_2 and (phosphorene, germanene, borophene) hybrid structure on the performance of an SPR biosensor for detection of bacteria. Opt. Rev. 31, 615–624.

Demchenko, A.P., 2005. The problem of self-calibration of fluorescence signal in microscale sensor systems. Lab Chip 5 (11), 1210–1223.

Fu, X., Tan, W., Song, Q., Pei, H., Li, J., 2022. BRCA1 and breast cancer: molecular mechanisms and therapeutic strategies. Front. Cell Dev. Biol. 10, 813457.

Gracias, D.T., Stelekati, E., Hope, J.L., Boesteanu, A.C., Doering, T.A., Norton, J., Mueller, Y.M., Fraietta, J.A., Wherry, E.J., Turner, M., Katsikis, P.D., 2013. The microRNA miR-155 controls CD8(+) T cell responses by regulating interferon signaling. Nat. Immunol. 14 (6), 593–602.

Gross, E., Arnold, N., Goette, J., Schwarz-Boeger, U., Kiechle, M., 1999. A comparison of BRCA1 mutation analysis by direct sequencing, SSCP and DHPLC. Hum. Genet. 105 (1–2), 72–78.

Han, C., Xu, X., Zhang, C., Yan, D., Liao, S., Zhang, C., Kong, L., 2021. Cytochrome c light-up graphene oxide nanosensor for the targeted self-monitoring of mitochondria-mediated tumor cell death. Biosens. Bioelectron. 173, 112791.

Han, Y.J., Zhang, J., Lee, J.H., Mason, J.M., Karginova, O., Yoshimatsu, T.F., Hao, Q., Hurley, I., Brunet, L.P., Prat, A., Prasanth, K.V., Gack, M.U., Olopade, O.I., 2021. The

BRCA1 pseudogene negatively regulates antitumor responses through inhibition of innate immune defense mechanisms. Cancer Res. 81 (6), 1540–1551.

Huang, X., Song, J., Yung, B.C., Huang, X., Xiong, Y., Chen, X., 2018. Ratiometric optical nanoprobes enable accurate molecular detection and imaging. Chem. Soc. Rev. 47 (8), 2873–2920.

Huang, Y., Zhang, Q., Lam, C.Y.K., Li, C., Yang, C., Zhong, Z., Zhang, R., Yan, J., Chen, J., Yin, B., Wong, S.H.D., Yang, M., 2024. An aggregation-induced emission-based dual emitting nanoprobe for detecting intracellular pH and unravelling metabolic variations in differentiating lymphocytes. ACS Nano 18 (24), 15935–15949.

Huo, X.-L., Lu, H.-J., Xu, J.-J., Zhou, H., Chen, H.-Y., 2019. Recent advances of ratiometric electrochemiluminescence biosensors. J. Mater. Chem. B 7 (42), 6469–6475.

Jia, Q.Q., Ji, H.M., Bai, X., 2019. Selective sensing property of triclinic WO nanosheets towards ultra-low concentration of acetone. J. Mater. Sci. Mater. Electron. 30 (8), 7824–7833.

Jiang, S., Butler, S., Bianco, E., Restrepo, O.D., Windl, W., Goldberger, J.E., 2014. Improving the stability and optical properties of germanane via one-step covalent methyl-termination. Nat. Commun. 5 (1), 3389.

Khazaei, M., Hosseini, M.S., Haghighi, A.M., Misaghi, M., 2023. Nanosensors and their applications in early diagnosis of cancer. Sens. Biosens. Res. 41, 100569.

Li, H., Wu, J., Yin, Z., Zhang, H., 2014. Preparation and applications of mechanically exfoliated single-layer and multilayer MoS_2 and WSe_2 nanosheets. Acc. Chem. Res. 47 (4), 1067–1075.

Li, Y., Liu, G., Cheng, S., Zhang, J., Yao, X., Xie, X., Xu, C., Tang, Y., Wang, X., Tang, B., 2025. Cellular redox regulation and fluorescence imaging. Chem. Rev. 125 (16), 7725–7810.

Luo, X., Sun, J., Kong, D., Lei, Y., Gong, F., Zhang, T., Shen, Z., Wang, K., Luo, H., Xu, Y., 2023. The role of germanium in diseases: exploring its important biological effects. J. Transl. Med. 21 (1), 795.

Morimitsu, Y., Matsuno, H., Oda, Y., Yamamoto, S., Tanaka, K., 2022. Direct visualization of cooperative adsorption of a string-like molecule onto a solid. Sci. Adv. 8 (41) eabn6349.

Reza Rezapour, M., Biel, B., 2022. DNA/RNA sequencing using germanene nanoribbons via two dimensional molecular electronic spectroscopy: an ab initio study. Nanoscale 14 (13), 5147–5153.

Rohaizad, N., Mayorga-Martinez, C.C., Fojtů, M., Latiff, N.M., Pumera, M., 2021. Two-dimensional materials in biomedical, biosensing and sensing applications. Chem. Soc. Rev. 50 (1), 619–657.

Ruan, Z., Yue, L., Liu, B., Kim, E., Chen, X., Li, J., Jang, H., Lin, Z., Li, M., Peng, X., 2025. Visualizing pulmonary pathologies using smart molecular fluorescent probes. Coord. Chem. Rev. 545, 217025.

Ryder, C.R., Wood, J.D., Wells, S.A., Hersam, M.C., 2016. Chemically tailoring semiconducting two-dimensional transition metal dichalcogenides and black phosphorus. ACS Nano 10 (4), 3900–3917.

Samstein, R.M., Krishna, C., Ma, X., Pei, X., Lee, K.W., Makarov, V., Kuo, F., Chung, J., Srivastava, R.M., Purohit, T.A., Hoen, D.R., Mandal, R., Setton, J., Wu, W., Shah, R., Qeriqi, B., Chang, Q., Kendall, S., Braunstein, L., Weigelt, B., Blecua Carrillo Albornoz, P., Morris, L.G.T., Mandelker, D.L., Reis-Filho, J.S., de Stanchina, E., Powell, S.N., Chan, T.A., Riaz, N., 2021. Mutations in BRCA1 and BRCA2 differentially affect the tumor microenvironment and response to checkpoint blockade immunotherapy. Nat. Cancer 1 (12), 1188–1203.

Sharma, A., Verwilst, P., Li, M., Ma, D., Singh, N., Yoo, J., Kim, Y., Yang, Y., Zhu, J.H., Huang, H., Hu, X.L., He, X.P., Zeng, L., James, T.D., Peng, X., Sessler, J.L., Kim, J.S., 2024. Theranostic fluorescent probes. Chem. Rev. 124 (5), 2699–2804.

Špringer, T., Bocková, M., Slabý, J., Sohrabi, F., Čapková, M., Homola, J., 2025. Surface plasmon resonance biosensors and their medical applications. Biosens. Bioelectron. 278, 117308.

Tan, C., Xie, G., Wu, S., Song, C., Zhang, J., Yi, X., Wang, J., Tang, H., 2024. Simultaneous detection of breast cancer biomarkers circROBO1 and BRCA1 based on a CRISPR-Cas13a/Cas12a system. Biosens. Bioelectron. 258, 116373.

Tang, J., Zhang, Y., Liu, Y., Liu, D., Qin, H., Lian, N., 2019. Carbon quantum dots as a fluorophore for “inner filter effect” detection of metronidazole in pharmaceutical preparations. RSC Adv. 9 (65), 38174–38182.

Tian, H., Jaquins-Gerstl, A., Munro, N., Trucco, M., Brody, L.C., Landers, J.P., 2000. Single-strand conformation polymorphism analysis by capillary and microchip electrophoresis: a fast, simple method for detection of common mutations in BRCA1 and BRCA2. Genomics 63 (1), 25–34.

Wallace, A.J., 2016. New challenges for BRCA testing: a view from the diagnostic laboratory. Eur. J. Hum. Genet. 24 (1), S10–S18.

Wang, X., Ding, Q., Groleau, R.R., Wu, L., Mao, Y., Che, F., Kotova, O., Scanlan, E.M., Lewis, S.E., Li, P., Tang, B., James, T.D., Gunnlaugsson, T., 2024. Fluorescent probes for disease diagnosis. Chem. Rev. 124 (11), 7106–7164.

Wilkinson, L., Gathani, T., 2022. Understanding breast cancer as a global health concern. Br. J. Radiol. 95 (1130), 20211033.

Wu, B., Qi, L., Chiang, H.-C., Pan, H., Zhang, X., Greenbaum, A., Stark, E., Wang, L.-J., Chen, Y., Haddad, B.R., Clagett, D., Isaacs, C., Elledge, R., Horvath, A., Hu, Y., Li, R., 2023. BRCA1 deficiency in mature CD8+ T lymphocytes impairs antitumor immunity. J. Immunother. Cancer 11 (2), e005852.

Wu, J., Liu, H., Chen, W., Ma, B., Ju, H., 2023. Device integration of electrochemical biosensors. Nat. Rev. Bioeng. 1 (5), 346–360.

Xue, T., Bongu, S.R., Huang, H., Liang, W., Wang, Y., Zhang, F., Liu, Z., Zhang, Y., Zhang, H., Cui, X., 2020. Ultrasensitive detection of microRNA using a bismuthene-enabled fluorescence quenching biosensor. Chem. Commun. 56 (51), 7041–7044.

Yadav, P.K., Kumar, A., Upadhyay, S., Kumar, A., Srivastava, A., Srivastava, M., Srivastava, Srivastava, S.K., 2024. 2D material–based surface plasmon resonance biosensors for applications in different domains: an insight. Microchim. Acta 191 (7), 1–30.

Yıldır, M.H., Kurtay, G., Bouali, W., Genç, A.A., Erk, N., 2024. Redefining precision in cancer treatment: a novel electrochemical approach using bimetal oxide composites for niraparib quantification. Microchem. J. 196, 109618.

Yuan, J., Najmaei, S., Zhang, Z., Zhang, J., Lei, S., Ajayan, P.M., Yakobson, B.I., Lou, J., 2015. Photoluminescence quenching and charge transfer in artificial heterostacks of monolayer transition metal dichalcogenides and few-layer black phosphorus. ACS Nano 9 (1), 555–563.

Zhang, Q., Yin, B., Hao, J., Ma, L., Huang, Y., Shao, X., Li, C., Chu, Z., Yi, C., Wong, S.H.D., Yang, M., 2023a. An AIEgen/graphene oxide nanocomposite (AIEgen@GO)-based two-stage “turn-on” nucleic acid biosensor for rapid detection of SARS-CoV-2 viral sequence. Aggregate 4 (1), e195.

Zhang, Q., Yin, B., Huang, Y., Gu, Y., Yan, J., Chen, J., Li, C., Zhang, Y., Wong, S.H.D., Yang, M., 2023b. A dual “turn-on” biosensor based on AIE effect and FRET for in situ detection of miR-125b biomarker in early alzheimer's disease. Biosens. Bioelectron. 230, 115270.

Zhang, X., Du Rietz, A., Hu, J., Brommesson, C., Wu, X., Uvdal, K., Hu, Z., 2021. A ratiometric fluorogenic nanoprobe for real-time quantitative monitoring of lysosomal pH. Sens. Actuators B-Chem. 345, 130350.

Zhu, C., Chen, Z., Gao, S., Goh, B.L., Samsudin, I.B., Lwe, K.W., Wu, Y., Wu, C., Su, X., 2019. Recent advances in non-toxic quantum dots and their biomedical applications. Prog. Nat. Sci. Mater. Int. 29 (6), 628–640.